Twisted molecular wires polarize spin currents at room temperature

Chih-Hung Ko[a], Qirong Zhu[b], Francesco Tassinari[b], George Bullard[a], Peng Zhang[a], David N. Beratan[a,1], Ron Naaman[b,1], and Michael J. Therien[a,1]

[a]Department of Chemistry, Duke University, Durham, NC 27708; and [b]Department of Chemical and Biological Physics, Weizmann Institute of Science, Rehovot 76100, Israel

Edited by Michael Wasielewski, Department of Chemistry, Northwestern University, Evanston, IL; received September 1, 2021; accepted December 17, 2021

A critical spintronics challenge is to develop molecular wires that render efficiently spin-polarized currents. Interplanar torsional twisting, driven by chiral binucleating ligands in highly conjugated molecular wires, gives rise to large near-infrared rotational strengths. The large scalar product of the electric and magnetic dipole transition moments ($\vec{\mu}_{ij} \cdot \vec{m}_{ij}$), which are evident in the low-energy absorptive manifolds of these wires, makes possible enhanced chirality-induced spin selectivity–derived spin polarization. Magnetic-conductive atomic force microscopy experiments and spin-Hall devices demonstrate that these designs point the way to achieve high spin selectivity and large-magnitude spin currents in chiral materials.

CISS effect | chirality induction | spin polarization | molecular wire | spin current

Spintronics offers exciting possibilities in applications that include information storage and magnetic sensing with reduced power consumption (1). Molecular organic semiconductors offer tremendous potential for electron spin transmission, as well as controlling spin decoherence and relaxation times (2). These opportunities derive in part from the fact that light-atom–based organic compositions have intrinsically weaker spin–orbit coupling (SOC) and hyperfine interactions than conventional inorganic semiconductors; such properties have enabled advances that include spin-polarized organic light-emitting diodes (3), organic spin valves (4), and spin-photovoltaic cells (5).

While organic molecules have small SOCs, the recently discovered chirality-induced spin selectivity (CISS) effect provides a new approach to control spins in molecules (6). Numerous experiments show that chiral molecules act as spin filters in electron transport. The same is true when an electric field is applied across a chiral molecule and induces charge reorganization. Because spin polarization accompanies charge polarization in chiral molecules (7), the CISS effect provides a potential solution to resolve the technological hurdles associated with injecting spin-polarized electrons from inorganic ferromagnets into organic molecules or vice versa; commonly, in such devices, the Schottky barrier limits spin injection efficiency and drives spin depolarization (8). Importantly, in this regard, the CISS effect has been used to generate spin polarizations approaching 100% under ambient conditions, even in the absence of a magnetic field (9). Because the CISS effect enables ambient temperature control of the electron spin through applied electrical and electromagnetic fields, it bears keen relevance to quantum information science, as it provides a potential pathway to generate coherent spin states (entangled electron pairs or spin qubits).

Spin-selective transmission made possible by the CISS effect has been demonstrated for chiral tunneling barriers fabricated from chiral molecules [e.g., oligopeptides (10, 11), L/D-cysteine (12), and oligonucleotides (13)], chiral nanoparticles [e.g., CdSe quantum dots (14) and chiral helicoidal three-dimensional metal organic frameworks (9)], and other materials (15, 16). Chiral organic structures that possess substantial charge mobilities and suppress spin dephasing offer the potential to realize materials that have dramatically enhanced CISS functionality. In this regard, we demonstrated recently that low-resistance molecular wires, with a mix of tunneling, hopping, and resonant transport mechanisms (17, 18), uniquely propagate spin-polarized currents (19). These exemplary compositions exploit conjugated zinc porphyrin wires (PZn_n), which manifest long spin-relaxation times (20), support highly delocalized hole and electron polaron states (21, 22), and feature extraordinarily low charge transport resistances (17, 18). In contrast to pioneering studies that have induced chirality in conjugated oligomers via H-bonding interactions (23), we demonstrate here that chiral twisted molecular wires can be engineered with conjugated PZn_n oligomers through coordination of chiral binucleating ligands; this strategy integrates both spin-polarizing and spin-propagating functionality in a single conductive organic framework, controls the handedness of the polarized spin, and thus regulates spin currents via the CISS mechanism.

Results and Discussion

Molecular Design and Circular Dichroism. Fig. 1 shows the structures of thiol-terminated meso-to-meso ethyne-bridged multi-[(porphinato)Zn] oligomers PZn_nSAc (n = 1 to 4), along with binucleating ligands that feature axial chirality (B_R and B_S)

Significance

In contrast to conventional electronics, spintronics devices exploit the electron spin as an additional degree of freedom. The chirality-induced spin selectivity (CISS) effect, in which chiral molecules act as spin filters in electron transport, provides a pathway to control spins in molecules. We describe an approach that integrates both spin-polarizing and spin-propagating functionality into organic structures that feature low charge transport resistances. Binding chiral ligands to molecular wires controls polarized spin handedness, regulates spin currents, generates large NIR rotational strengths, and provides a mechanism to flip the favored spin orientation for spin transmission through chiral organic molecules. This work points the way to materials that provide both high spin selectivity and large-magnitude spin currents via the CISS mechanism.

Author contributions: C.-H.K. and M.J.T. designed research; C.-H.K., Q.Z., F.T., G.B., and P.Z. performed research; C.-H.K., Q.Z., F.T., G.B., and P.Z. analyzed data; and C.-H.K., P.Z., D.N.B., R.N., and M.J.T. wrote the paper.

The authors declare no competing interest.

This article is a PNAS Direct Submission.

[1]To whom correspondence may be addressed. Email: david.beratan@duke.edu, ron.naaman@weizmann.ac.il, or michael.therien@duke.edu.

This article contains supporting information online at http://www.pnas.org/lookup/suppl/doi:10.1073/pnas.2116180119/-/DCSupplemental.

Published February 3, 2022.

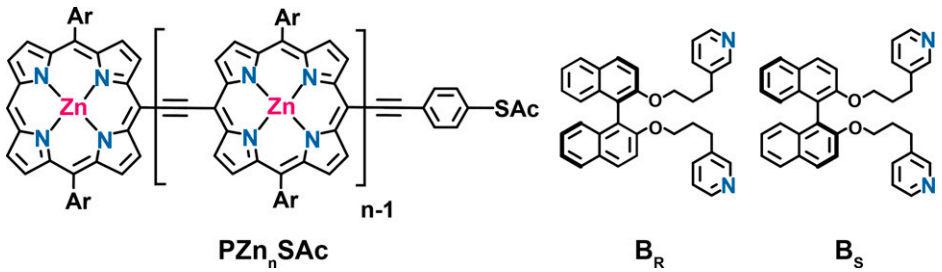

Fig. 1. Chemical structures of PZn$_n$SAc and chiral binucleating ligands B$_R$ and B$_S$. Ar, 2′,6′-bis(3,3-dimethyl-l-butyloxy)phenyl; Ac, acetate.

derived from 1,1′-bi(2-naphthol); syntheses and characterization of these compositions are detailed in the *SI Appendix*. Electronic absorption spectra of PZn$_{1–4}$SAc in CH_2Cl_2 solvent are displayed in Fig. 2*A*; addition of the B$_S$ ligand results in a bathochromic shift of the PZn$_{1–4}$SAc low-energy, long-conjugated axis (*x*-) polarized absorption manifold (Fig. 2*B*) (21, 22, 24–30), and modest hyperchromism, consistent with axial ligation of (porphinato)zinc chromophores that feature an a_{2u}-derived highest occupied molecular orbital (31). Table 1 highlights the magnitudes of the association constants (*K*) for these B$_{R/S}$ ligands relative to those determined for pyridine for these PZn$_n$SAc molecular wires. Note that $K_{BR/S}/K_{pyridine}$ is amplified with increasing PZn$_n$SAc conjugation length, with the B$_{R/S}$ association constant determined for PZn$_4$SAc (5.61×10^5) two orders of magnitude larger than that for pyridine (7.66×10^3). Job plot analyses of ligand association (*SI Appendix*) unveil PZn$_n$SAc:B$_{R/S}$ binding stoichiometries as anticipated (Table 1), congruent with the binucleating nature of these chiral ligands and cooperative binding (Table 1) (32).

These twisted chiral structures that result from B$_R$ or B$_S$ ligand coordination express differential absorption of left- and right-handed circularly polarized light; circular dichroism (CD) spectra of PZn$_n$SAc:B$_{R/S}$ wires highlight visible (Vis)–near-infrared (NIR) signals that not only intensify with increasing conjugation length, but corresponding long-wavelength molar ellipticities that dramatically red shift as the chain lengths grow (Fig. 2*C*) (33). B$_{R/S}$ ligands absorb at wavelengths <360 nm (*SI Appendix*) and display symmetric CD signals that depend on absolute chirality. Addition of B$_R$ or B$_S$ to PZn$_{2–4}$SAc beget similarly symmetric CD signals between 360 and 900 nm (Fig. 2*C*); note that the Cotton effect is absent for PZn$_1$SAc, underscoring that PZn$_n$ wire chirality is established via the engineered chiral interplanar torsional twist of adjacent planar PZn macrocycles in PZn$_{2–4}$SAc. Fig. 3 displays a B3LYP/def2-SVP–derived structure of PZn$_4$SAc coordinated by two B$_S$ units (34), highlighting the chiral twisting along the molecular wire induced by B$_{R/S}$ ligand coordination.

Fig. 2*C* highlights as well that the magnitude of the Cotton effect increases with increasing PZn$_n$ conjugation length. Several aspects of these data are noteworthy. Over the 350 to 550 nm (B-state–dominated) regime, it is evident that the magnitude of Δε, the molar ellipticity, measured at the PZn$_{2–4}$SAc-B$_{R/S}$ electronic absorption maxima, displays conjugation length dependences that differ from those characteristic of their extinction coefficient maxima (Fig. 2*B*). Likewise, over the wavelength domain that spans the PZn$_n$ Q-state absorptive manifold (550 to 900 nm), the maximal Q-state Δε value is seen to increase by a factor of two with each additional PZn unit in PZn$_{2–4}$SAc-B$_{R/S}$ (Fig. 2*C*), a more dramatic conjugation length dependence than that exhibited by the corresponding electronic absorptive extinction coefficient maxima (Fig. 2*B*) in this spectral region.

As the integrated oscillator strength (*f*) reflects the transition probability in a linear absorption spectrum (Eq. **1**, where ε is the experimental extinction coefficient and υ is the energy [in wave numbers] of the absorption) and is proportional to the

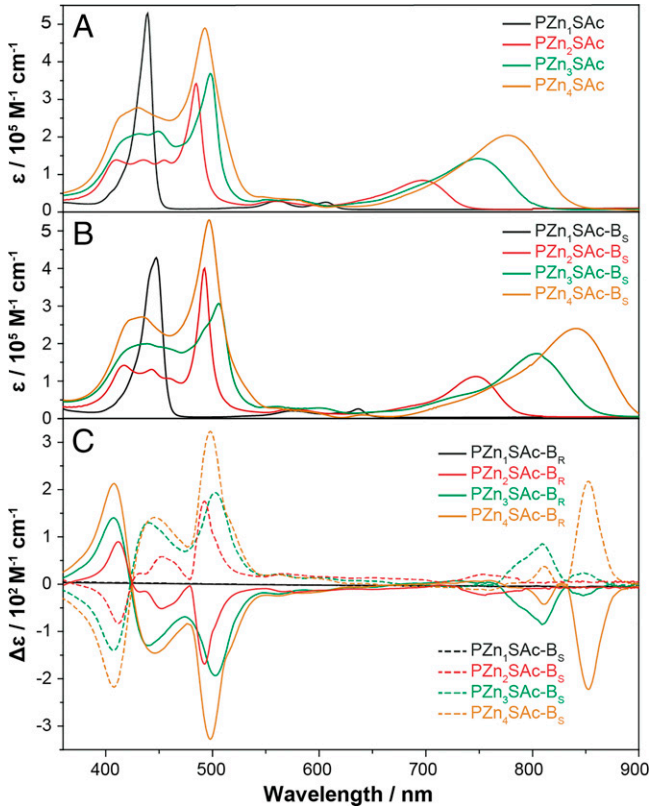

Fig. 2. Electronic absorption and CD spectra of PZn$_{1–4}$SAc. (*A*) Comparative electronic absorption spectra of PZn$_1$SAc (black), PZn$_2$SAc (red), PZn$_3$SAc (green), and PZn$_4$SAc (brown) recorded in CH_2Cl_2 solvent. (*B*) Electronic absorption spectra of PZn$_1$SAc (black), PZn$_2$SAc (red), PZn$_3$SAc (green), and PZn$_4$SAc (brown) in the presence of 10 equivalents of B$_S$. (*C*) CD spectra of PZn$_1$SAc (black), PZn$_2$SAc (red), PZn$_3$SAc (green), and PZn$_4$SAc (brown) in the presence of 10 equivalents B$_R$ (solid line) or B$_S$ (dashed line). Additional details are provided in the *SI Appendix*.

Table 1. Association constants (*K*) and stoichiometry of PZn$_n$SAc ligand coordination

Molecular wire	*K* (M^{-1})*		PZn$_n$SAc:B$_{R/S}$ stoichiometry†
	B$_{R/S}$ ligand	Pyridine	
PZn$_1$SAc	2.71×10^4	1.82×10^3	N/A
PZn$_2$SAc	1.86×10^5	2.47×10^3	1:1
PZn$_3$SAc	3.84×10^5	7.57×10^3	1:1.5
PZn$_4$SAc	5.61×10^5	7.66×10^3	1:2

N/A, not applicable.
*Association constants were ascertained from Hill Plots determined from B$_{R/S}$ or pyridine ligand titration data acquired in CH_2Cl_2 solvent.
†Ligand binding stoichiometries were determined from Job plot analyses.

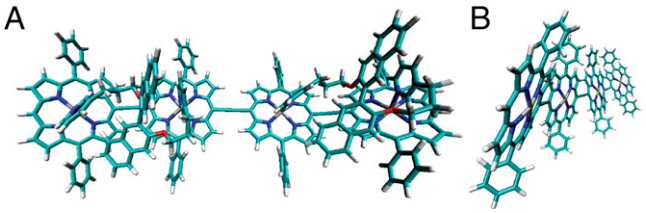

Fig. 3. B3LYP/def2-SVP-computed (34) energy minimized conformation of $PZn_4SAc\text{-}B_R$. (*A*) Front view of $PZn_4SAc\text{-}B_R$. (*B*) Side view of $PZn_4SAc\text{-}B_R$. Porphyrin meso-phenyl substituents and the protected thiol-terminal SAc group of $PZn_4SAc\text{-}B_R$ are omitted for clarity in *A* and *B*; the binucleating B_R ligands are also removed for simplicity in *B*.

square of the transition dipole moment $\vec{\mu}_{ij}$, the rotational strength (R) corresponds to the integral described by Eq. **2**, and is proportional to the magnitude of the scalar product $\vec{\mu}_{ij} \cdot \vec{m}_{ij}$, where $\vec{m}_{ij}$ is the magnetic transition moment. One convenient way to express R is in terms of a reduced rotational strength [R] (Eq. **3**); here, μ_B is the Bohr magneton (0.927×10^{-20} cgs) and μ_D is the Debye (10^{-18} cgs) (35).

$$f = 4.32 \times 10^{-9} \int \varepsilon \, dv \propto \vec{\mu}_{ij}{}^2. \quad [1]$$

$$R = 2.297 \times 10^{-39} \int \Delta\varepsilon \, dv \propto \vec{\mu}_{ij} \cdot \vec{m}_{ij} = \mu_{ij}^x m_{ij}^x + \mu_{ij}^y m_{ij}^y + \mu_{ij}^z m_{ij}^z. \quad [2]$$

$$[R] = \frac{100R}{\mu_B \mu_D} = (1.08 \times 10^{40})R. \quad [3]$$

Fig. 4*A* describes the dependence of the absolute value of |[R]|, as a function of $PZn_{2\text{–}4}SAc\text{-}B_{R/S}$ conjugation length, for the B-state manifold, the Q-state manifold, and the 360 to 900 nm spectral region (B + Q), while Fig. 4*B* highlights the correlation between f(Q) and |[R]|(Q) as a function of PZn_n wire length. This latter plot underscores that the $\vec{\mu}_{ij} \cdot \vec{m}_{ij}$ product increases with increasing conjugation length more dramatically than does $\vec{\mu}_{ij}{}^2$ within the Q-state manifold. These data thus indicate that either the magnetic dipole transition moment grows more rapidly than the electric dipole transition moment with increasing conjugation length or that the $\vec{\mu}_{ij}$ and $\vec{m}_{ij}$ alignment increases with molecular wire length and diminishing optical band gap in these $PZn_nSAc\text{-}B_{R/S}$ structures. The fact that $B_{R/S}$ ligation fixes the range of torsional angles between adjacent PZn macrocycles ($23 \pm 2°$) and the thermally weighted torsional angle distribution between $B_{R/S}$ ligated PZn_2 units in $PZn_{n4}SAc\text{-}B_{R/S}$ is dominated by conformers featuring similar angles (27, 36, 37) argues strongly for the former scenario.

Computational Simulation. Time-dependent density-functional theory methods (B3LYP, MN15, and CAM-B3LYP functionals) were used to compute the $S_0 \rightarrow S_1$ electric and magnetic transition dipoles and the rotational strengths for the $PZn_2\text{-}B_{R/S}$, *cis*–$PZn_4\text{-}B_{R/S}$, and *trans*–$PZn_4\text{-}B_{R/S}$ (*SI Appendix*); the *cis* and *trans* configurations refer to the spatial relationship of the two $B_{R/S}$ ligands that bind the PZn_2 units of PZn_4. Fig. 5 highlights the electronic and magnetic transition densities for *cis*–$PZn_4\text{-}B_{R/S}$ and the spatial arrangement of electric (μ, red) and magnetic (m, blue) transition moments computed at the ground state equilibrium structure. These panels emphasize the importance of the torsional angle between the two $PZn_2\text{-}B_{R/S}$ units in *cis*–$PZn_4\text{-}B_{R/S}$ in determining the magnitudes of the magnetic transition dipole and the $\vec{\mu}_{ij} \cdot \vec{m}_{ij}$ product for *cis*–$PZn_4\text{-}B_{R/S}$. These relationships are detailed in the *SI Appendix* and underscore that the large rotatory strength observed for $PZn_4SAc\text{-}B_{R/S}$ is correlated closely with the magnitude of the x component of the magnetic transition dipole moment (m_{ij}^x, Eq. **2**). Because the electric transition dipole is almost entirely concentrated in the x direction regardless of the torsional angle between $PZn_2\text{-}B_{R/S}$ units of *cis*–$PZn_4\text{-}B_{R/S}$, controlling the magnitude of this angle sensitively modulates rotatory strength and sign, as the $\mu_{ij}^x m_{ij}^x$ term (Eq. **2**) plays the dominant role in determining R. Fig. 6 depicts the computed electric and magnetic transition dipoles, the rotatory strength, and the relative energies of *cis*–$PZn_4\text{-}B_{R/S}$ and *trans*–$PZn_4\text{-}B_{R/S}$ conformers along the torsional coordinate (*SI Appendix*). Note that the Boltzmann weighted rotatory strengths for *cis*–$PZn_4\text{-}B_{R/S}$ and *trans*–$PZn_4\text{-}B_{R/S}$ conformers predict a reduced rotational strength [R] for the $PZn_4\text{-}B_{R/S}$ Q-state manifold of ~100, within a factor of two of that determined experimentally (Fig. 4*B*). These experimental and computational data that characterize the chiro-optic properties associated with the low-energy electronic states of chiral $PZn_nSAc\text{-}B_{R/S}$ wires, coupled with the fact that the magnetic dipole operator is the same as the one that factors into the SOC Hamiltonian, suggest a pathway to realize SOCs that are large relative to those determined for soft material benchmarks (10–13) and thus facilitate enhanced CISS-derived spin polarization. While there is no theoretical model that explicitly links chiro-optic response with charge polarization–induced spin-polarization magnitudes in a comprehensive and fully quantitative way, a qualitative connection along these lines has been noted (38–42).

Electron Spin Polarization. The utility of PZn_4SAc and $PZn_4SAc\text{-}B_{R/S}$ wires to generate and transmit spin-polarized currents was evaluated using magnetic-conductive atomic force microscopy (mC-AFM), a well-established method for measuring spin-selective conduction through self-assembled monolayers (SAMs) of chiral molecules (19). In these experiments, the substrate is

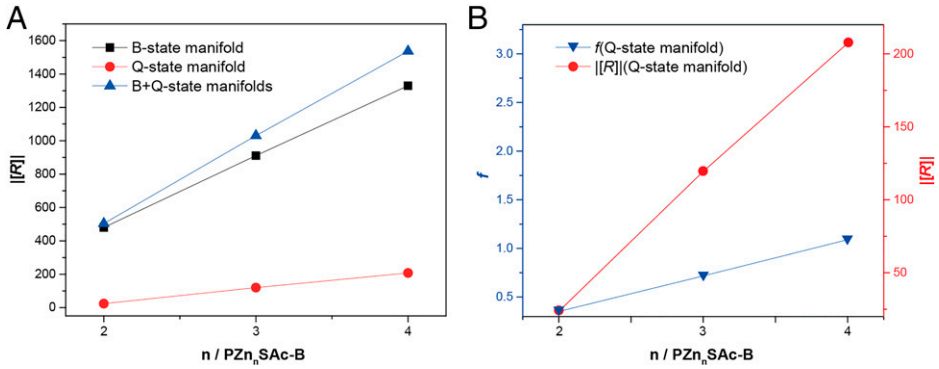

Fig. 4. Rotational strength of $PZn_{2\text{–}4}SAc$. (*A*) The relationship between the absolute reduced rotational strength [R] and $PZn_{2\text{–}4}SAc$ conjugation length over the B-state manifold, the Q-state manifold, and the 360 to 900 nm spectral region (B + Q). (*B*) Correlation between absorptive oscillator strength f and the absolute reduced rotational strength [R] over the Q-state manifold for $PZn_{2\text{–}4}SAc$ structures.

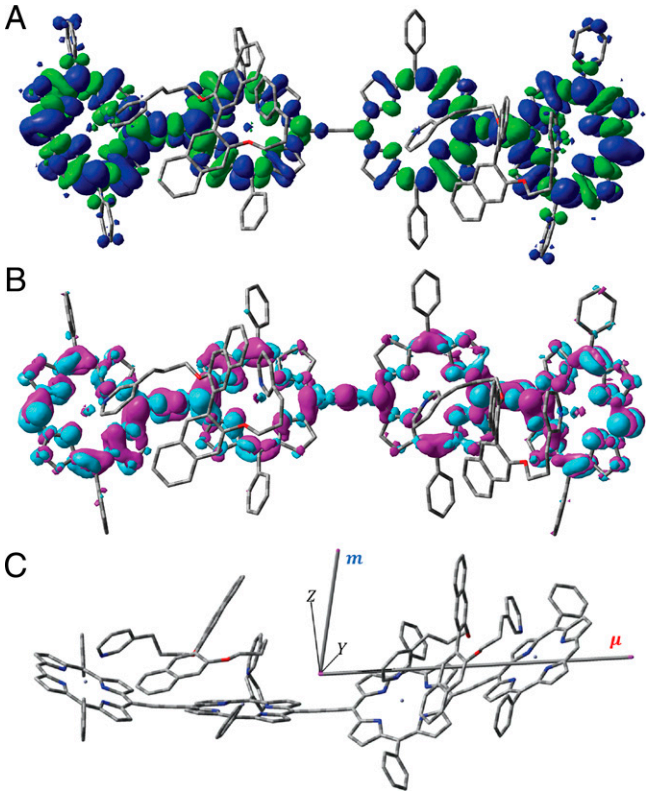

Fig. 5. CAM-B3LYP–computed properties of the $S_0 \rightarrow S_1$ (*A*) electric transition and (*B*) magnetic transition densities of *cis*–PZn_4-$B_{R/S}$ determined at the density functional theory–optimized ground state energy minimum (isosurface values = 0.004 atomic unit). (*C*) The spatial arrangement of electric (μ, red) and magnetic (*m*, blue) transition moments computed at the ground state equilibrium structure.

biased relative to the grounded tip. Note that when the substrate is negatively biased electrons are injected from the majority spin density of states, just below the Fermi level, while when the substrate is positively biased, spins are injected to the minority density of states just above the Fermi level. Hence, for the same substrate magnetization, the electrons injected out have one spin, while those that are injected in from the monolayer have the opposite spin. SAMs of PZn_4SAc, PZn_4SAc-B_R, and PZn_4SAc-B_S were formed on Ti/Ni/Au (10:120:8 nm) thin layers. Note that relative to thiol-Au bonding, the $B_{R/S}$ pyridyl functional groups have a weak interaction with the Au surface; any uncoordinated B_R or B_S ligands on the gold surface can be readily removed following SAM preparation. A Pt-coated AFM tip was used to measure the spin current passing through the SAMs as the substrate was biased potentiometrically between −2.0 V and 2.0 V; these studies utilize a permanent magnet, placed underneath the substrate, which controls the spin alignment in the Ni substrate layer either parallel or antiparallel to the current direction (Fig. 7*A*).

Fig. 7 *B*–*F* display the average current-voltage (*I*-*V*) responses obtained in these mC-AFM experiments when the Ni spins are either pointing up or down; the *SI Appendix* provides the corresponding statistical data. Fig. 7*B* highlights the fact that achiral PZn_4SAc is incapable of generating a spin-polarized current, as no differences between the average *I*-*V* curves were evident when the direction of the magnetic field was changed. In contrast, mC-AFM probe measurements of PZn_4SAc-B_R and PZn_4SAc-B_S films (Fig. 7 *C* and *D*) display highly antisymmetric *I*-*V* responses and indicate unequivocally that the conduction of one spin is dominant as current flows from the substrate to the AFM tip, while the opposite spin is dominant as current flows in the other direction for these systems. The extent of spin polarization, $(I_{up} - I_{down})/(I_{up} + I_{down}) \times 100\%$, where I_{up} and I_{down} are the currents measured with magnetic north pole up and down, indicates spin polarizations for PZn_4SAc-B_R and PZn_4SAc-B_S of ∼32% at a 2 V bias (*SI Appendix*). These results demonstrate that the induced chirality evidenced for PZn_4SAc-B_R and PZn_4SAc-B_S in solution can be preserved in these SAMs. Fig. 7 *E* and *F* underscore that the relationship between spin conduction and the Ni magnetization can be reversed; simple incubation of the Fig. 7 *C* and *D* SAMs with CH_2Cl_2 solutions of binucleating ligands of the opposite chirality flips SAM chirality (PZn_4SAc-$B_S \rightarrow PZn_4SAc$-B_R, Fig. 7 *E*; PZn_4SAc-$B_R \rightarrow PZn_4SAc$-B_S, Fig. 7*F*) on the Ti/Ni/Au substrate. This demonstration of spin current switching that regulates the favored spin orientation for transmission through these chiral molecular wires via ligand-modulated chirality induction was further investigated in spin-polarization Hall devices.

SAMs of PZn_4SAc-B_R and PZn_4SAc-B_S were adsorbed on an Au-coated GaN/AlGaN two-dimensional electron gas structure that is integrated in a spin-Hall device configuration (Fig. 8*A*) (43, 44). In this setup, a constant *I*-*V* is driven between the source (S) and drain (D) electrodes through the device, and the Hall voltage is measured between two Hall electrodes (H) along the direction perpendicular to the current flow. An applied electric field between the gate electrode and the device causes the SAM to be charge polarized. If this charge polarization is accompanied by spin polarization, spin polarization at the GaN/AlGaN/SAM interface generates a magnetic field capable of being detected by the Hall device (43) that results from the continuous nonequilibrium spin-polarized current that flows from the Au-coated GaN/AlGaN layer through the SAMs. The spin polarization that accompanies charge polarization in PZn_4SAc-B_R and PZn_4SAc-B_S SAMs was measured using sequential gate pulses from −50 to 50 V at 10-V intervals (Fig. 8*B*). Plotting these Hall voltages as a function of gate potential demonstrates an approximate linear relationship with the applied gate voltage. Note that the opposite signs of the slopes determined for PZn_4SAc-B_R and PZn_4SAc-B_S SAMs in these spin-Hall devices indicate opposite charge polarization–induced spin polarizations that depend strictly on the chirality of these molecular wires. Fig. 8*D* describes analogous data obtained when the SAMs of these spin-Hall devices are incubated with CH_2Cl_2 solutions of binucleating ligands having opposite chirality (*SI Appendix*). While the observed asymmetry in the gate voltage–dependent Hall voltage measurements of Fig. 8*D* likely arises

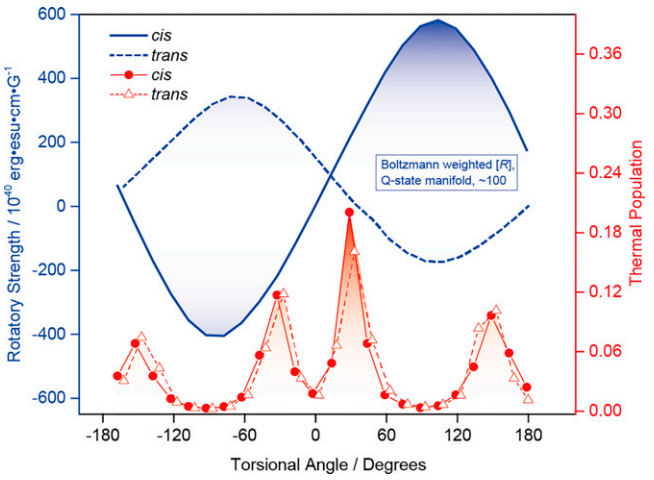

Fig. 6. CAM-B3LYP–computed torsional angle dependent rotatory strength *R* and thermal distribution of the PZn_4-$B_{R/S}$ structures. Circle and triangle symbols denote *cis*–PZn_4-$B_{R/S}$ and *trans*–PZn_4-$B_{R/S}$ torsional conformer thermal distributions, respectively, along the torsional coordinate.

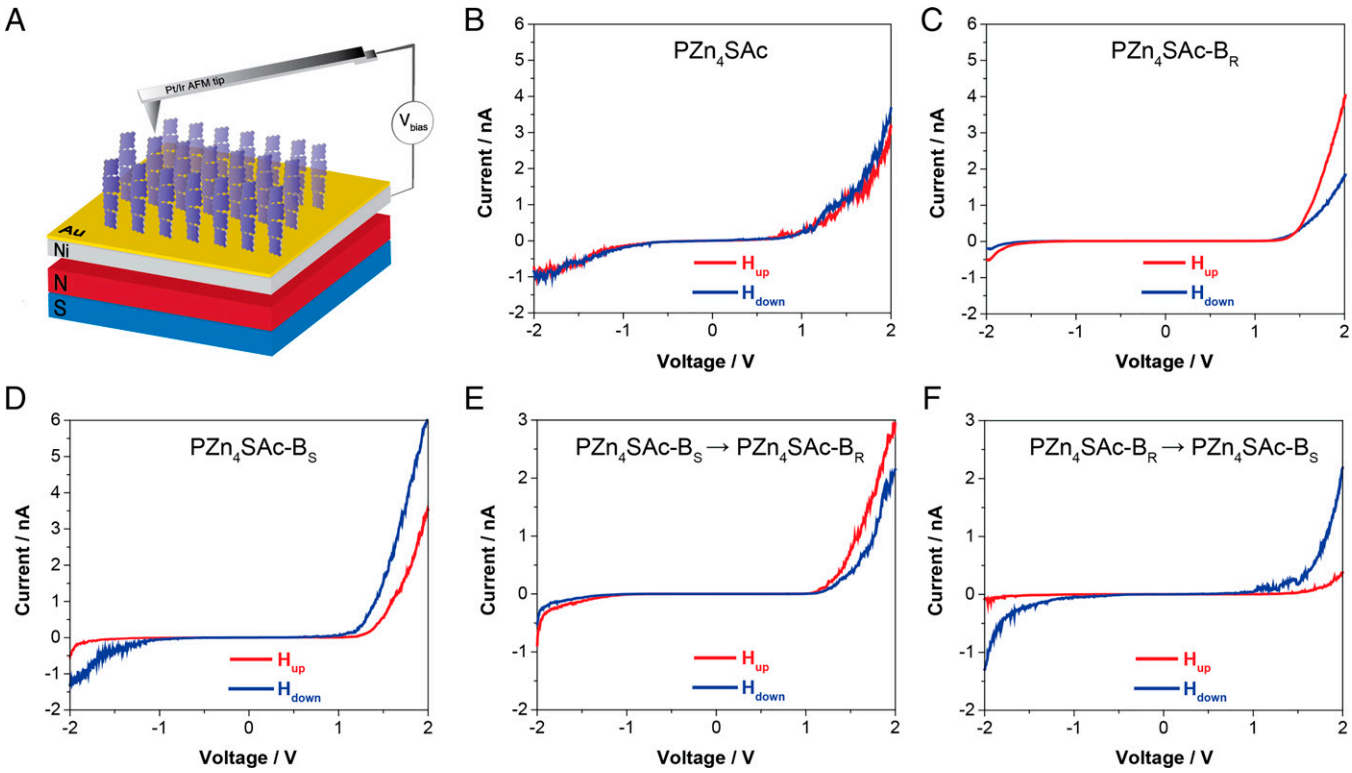

Fig. 7. Spin-dependent conduction through PZn_4SAc, $PZn_4SAc\text{-}B_R$, and $PZn_4SAc\text{-}B_S$ SAMs. (*A*) Schematic of the mC-AFM experimental setup. *I-V* curves obtained for (*B*) PZn_4SAc, (*C*) $PZn_4SAc\text{-}B_R$, (*D*) $PZn_4SAc\text{-}B_S$, (*E*) $PZn_4SAc\text{-}B_S \rightarrow PZn_4SAc\text{-}B_R$, and (*F*) $PZn_4SAc\text{-}B_R \rightarrow PZn_4SAc\text{-}B_S$, respectively, with the north pole of magnetic field pointing up (red line) or down (blue line) over a −2.0 to 2.0 V potentiometric window. $PZn_4SAc\text{-}B_S \rightarrow PZn_4SAc\text{-}B_R$ (*E*) and $PZn_4SAc\text{-}B_R \rightarrow PZn_4SAc\text{-}B_S$ (*F*) *I-V* responses were obtained by incubating the respective $PZn_4SAc\text{-}B_S$ (*D*) and $PZn_4SAc\text{-}B_R$ (*C*) devices in solutions of B_R and B_S ligands, enabling exchange of the chiral binucleating axial ligand with its opposite enantiomer on the as-formed SAM on the Ti/Ni/Au substrate of these devices. All the individual *I-V* dependences presented correspond to average responses determined from 110 consecutive sweeps.

from factors such as SAM rearrangements associated with the binucleating ligand equilibration process and incomplete ligand exchange, the Fig. 8*D* data clearly reveal $PZn_4SAc\text{-}B_S \rightarrow PZn_4SAc\text{-}B_R$ and $PZn_4SAc\text{-}B_R \rightarrow PZn_4SAc\text{-}B_S$ ligand induced chirality inversion (Fig. 8*C*), congruent with flipping the sign of the slope and the near-linear relation of the observed Hall voltage upon gate voltage magnitude, further substantiating analogous results observed in mC-AFM experiments.

Conclusion

In conclusion, this work demonstrates the utility of programmed chiral induction to realize low-resistance molecular wires that feature integrated spin-polarizing and spin-propagating functionality. This chiral induction strategy takes advantage of chiral binucleating ligands derived from 1,1′-bi(2-naphthol) (B_R and B_S ligands) and engenders high oscillator–strength long-wavelength PZn_nSAc absorbers with correspondingly intense chiroptical NIR spectral responses. These $PZn_nSAc\text{-}B_{R/S}$ systems not only possess NIR rotational strengths (R values) that are large with respect to established benchmarks (45) but define rare if not unique examples of processable, conjugated oligomers having large NIR molar ellipticities. A combination of electronic absorptive and CD spectral data indicates that the magnitude of the rotational strength increases markedly with increasing $PZn_nSAc\text{-}B_{R/S}$ conjugation length; in these structures, augmented oligomer conjugation gives rise not only to increasingly intense and red-shifted NIR absorptive manifolds but a CD signal that increases remarkably with increasing conjugation length faster than does $\vec{\mu}_{ij}^{\,2}$. Computational studies indicate that the large rotatory strengths are correlated closely with the magnitude of the x component of the magnetic transition dipole moment (m_{ij}^x) and indicate strategies to modulate rotatory strength and sign, as the $\mu_{ij}^x m_{ij}^x$ term dominates R and is extraordinarily sensitive to the magnitude of the torsional angle between adjacent PZn units in $PZn_nSAc\text{-}B_{R/S}$ systems.

Because $\vec{\mu}_{ij} \cdot \vec{m}_{ij}$ is very large in the low-energy absorptive manifolds of these compositions, this signature magneto-optic property highlights the potential to use these chiral molecular wires in spintronic applications. mC-AFM experiments and data acquired in spin-Hall devices for SAMs of $PZn_4SAc\text{-}B_R$ and $PZn_4SAc\text{-}B_S$ demonstrate that these compositions generate and transmit spin-polarized currents via the CISS mechanism, and that the favored spin orientation for transmission through these chiral molecular wires is opposite for these $PZn_4SAc\text{-}B_R$ and $PZn_4SAc\text{-}B_S$ structures. Simple ligand exchange reactions demonstrate an approach to flip favored spin orientation for spin transmission through chiral organic molecules, sharply contrasting approaches that have relied on temperature-induced conformational changes or electrical dipole inversion to modulate the nature of spin selectivity (39, 46). Because low-energy electronic states play critical roles in determining the magnitude of charge polarization–induced spin polarization and PZn_n compositions support high charge mobilities (22), these designs point the way to chiral materials that provide both high spin selectivity and large-magnitude spin currents via the CISS mechanism and chiral wires that enable coherent coupling between spin states.

Materials and Methods

Synthetic Materials. All manipulations were carried out under insert gas previously passed through an O_2 scrubbing tower packed with Schweizerhall R3-11 catalyst and a drying tower packed with Linde 3-Å molecular sieves. Air-

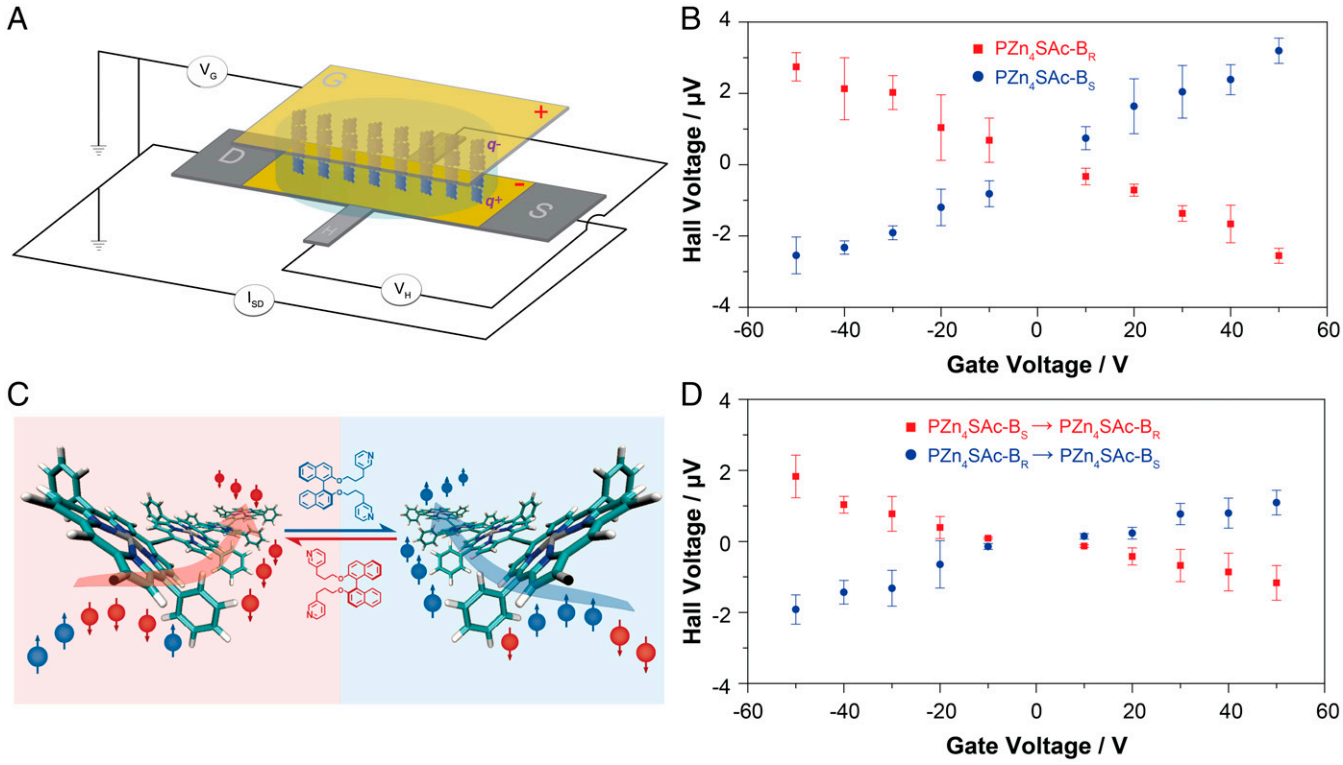

Fig. 8. Spin-polarization Hall device of $PZn_4SAc\text{-}B_{R/S}$. (*A*) Schematic of the spin-polarization Hall device used to measure the charge polarization–induced spin polarization driven by $PZn_4SAc\text{-}B_R$ and $PZn_4SAc\text{-}B_S$ SAMs. The top gate electrode (gold) is used to apply an electric field. The electrode is insulated from the electrolyte solution, and therefore, no faradaic current flows between the gate and the Hall device. In these Hall devices coated with $PZn_4SAc\text{-}B_R$ and $PZn_4SAc\text{-}B_S$ SAMs, a current (I_{SD}) is generated by the applied voltage between source (S) and drain (D) electrodes. Once the gate voltage (V_G) is applied, an electrical field (+, −) acts on the SAMs. If charge reorganization ($q+$, $q-$) in the SAM is accompanied by spin polarization, a magnetic field is generated that is detected by the device as a Hall voltage (V_H). (*B*) The relationship between Hall voltage and gate voltage observed for SAMs of $PZn_4SAc\text{-}B_R$ (red squares) and $PZn_4SAc\text{-}B_S$ (blue circles) SAMs assembling on the gold surface. (*C*) Schematic describing how ligand exchange reactions flip the favored spin orientation for spin transmission through chiral-conjugated zinc porphyrin wires. (*D*) The observed relationship between Hall voltage and gate voltage following exchange of the chiral binucleating ligand ($PZn_4SAc\text{-}B_S \rightarrow PZn_4SAc\text{-}B_R$, red squares) and ($PZn_4SAc\text{-}B_R \rightarrow PZn_4SAc\text{-}B_S$, blue circles) in these devices. Additional details are provided in the *SI Appendix*.

sensitive compounds were handled in a Braun 150-M glove box. Air-sensitive reactions were conducted by employing standard Schlenk technique. All reagents purchased from Sigma-Aldrich, TCI, Chem-Impex, and Thermo Fisher Scientific were used as received without further purification. All solvents utilized in this work were obtained from Thermo Fisher Scientific and Sigma-Aldrich (high-performance liquid chromatography grade). CH_2Cl_2 and tetrahydrofuran were dried from a PURE SOLV (Innovative Technology) solvent purification system with 4-Å molecular sieves and degassed by freeze-pump-thaw cycles.

General Characterization Instruments. Either a 400 or 500 MHz Bruker spectrometer was used to obtain NMR spectra for all synthesized compounds. Mass spectral data were obtained using a Brucker Autoflex matrix-assisted laser desorption/ionization time of flight system using a 2-(4-hydroxyphenylazo)benzoic acid (HABA) matrix. The Ti/Ni/Au (10:120:8 nm) thin layer substrates were employed in the measurement of spin polarization. Electronic absorption spectra were recorded on either a SHIMADZU UV-1700 UV-Vis or VARIAN Cary 5000 UV-Vis-NIR spectrophotometer. CD spectra were record on a model 435 AVIV CD and Applied Photophysics Chirascan Spectrometer.

Data Availability. All study data are included in the article and/or supporting information.

ACKNOWLEDGMENTS. C.-H.K., G.B., P.Z., D.N.B. and M.J.T. acknowledge the Center for Synthesizing Quantum Coherence, supported through the NSF (CHE-1925690), for funding this research. Q.Z., F.T., and R.N. acknowledge the Binational Science Foundation–NSF through grant no. 2015689 and the Minerva Foundation for research support. C.-H.K. is grateful to Duke University for a Graduate Program Nano-science Fellowship, and G. B. gratefully acknowledges the Fitzpatrick Institute of Photonics at Duke University for a John T. Chambers Scholars Award. M.J.T. is indebted to the John Simon Guggenheim Memorial Foundation for a research fellowship.

1. S. A. Wolf *et al.*, Spintronics: A spin-based electronics vision for the future. *Science* **294**, 1488–1495 (2001).
2. S. Sanvito, Molecular spintronics. *Chem. Soc. Rev.* **40**, 3336–3355 (2011).
3. Y.-H. Kim *et al.*, Chiral-induced spin selectivity enables a room-temperature spin light-emitting diode. *Science* **371**, 1129–1133 (2021).
4. V. A. Dediu, L. E. Hueso, I. Bergenti, C. Taliani, Spin routes in organic semiconductors. *Nat. Mater.* **8**, 707–716 (2009).
5. X. Sun *et al.*, A molecular spin-photovoltaic device. *Science* **357**, 677–680 (2017).
6. R. Naaman, D. H. Waldeck, Spintronics and chirality: Spin selectivity in electron transport through chiral molecules. *Annu. Rev. Phys. Chem.* **66**, 263–281 (2015).
7. R. Naaman, Y. Paltiel, D. H. Waldeck, Chiral molecules and the spin selectivity effect. *J. Phys. Chem. Lett.* **11**, 3660–3666 (2020).
8. H.-J. Jang, C. A. Richter, Organic spin-valves and beyond: Spin injection and transport in organic semiconductors and the effect of interfacial engineering. *Adv. Mater.* **29**, 1602739 (2017).
9. U. Huizi-Rayo *et al.*, An ideal spin filter: Long-range, high-spin selectivity in chiral helicoidal 3-dimensional metal organic frameworks. *Nano Lett.* **20**, 8476–8482 (2020).
10. A. Kumar *et al.*, Chirality-induced spin polarization places symmetry constraints on biomolecular interactions. *Proc. Natl. Acad. Sci. U.S.A.* **114**, 2474–2478 (2017).
11. F. Tassinari *et al.*, Enhanced hydrogen production with chiral conductive polymer-based electrodes. *J. Phys. Chem. A* **121**, 15777–15783 (2017).
12. S. P. Mathew, P. C. Mondal, H. Moshe, Y. Mastai, R. Naaman, Non-magnetic organic/inorganic spin injector at room temperature. *Appl. Phys. Lett.* **105**, 242408 (2014).
13. D. N. Beratan, R. Naaman, D. H. Waldeck, Charge and spin transport through nucleic acids. *Curr. Opin. Electrochem.* **4**, 175–181 (2017).
14. B. P. Bloom, V. Kiran, V. Varade, R. Naaman, D. H. Waldeck, Spin selective charge transport through cysteine capped CdSe quantum dots. *Nano Lett.* **16**, 4583–4589 (2016).
15. P. C. Mondal *et al.*, Chiral conductive polymers as spin filters. *Adv. Mater.* **27**, 1924–1927 (2015).

16. V. Kiran *et al.*, Helicenes—A new class of organic spin filter. *Adv. Mater.* **28**, 1957–1962 (2016).
17. Z. Li, T.-H. Park, J. Rawson, M. J. Therien, E. Borguet, Quasi-ohmic single molecule charge transport through highly conjugated meso-to-meso ethyne-bridged porphyrin wires. *Nano Lett.* **12**, 2722–2727 (2012).
18. R. C. Bruce, R. Wang, J. Rawson, M. J. Therien, W. You, Valence band dependent charge transport in bulk molecular electronic devices incorporating highly conjugated multi-[(porphinato)metal] oligomers. *J. Am. Chem. Soc.* **138**, 2078–2081 (2016).
19. G. Bullard *et al.*, Low-resistance molecular wires propagate spin-polarized currents. *J. Am. Chem. Soc.* **141**, 14707–14711 (2019).
20. J. Rawson, P. J. Angiolillo, P. R. Frail, I. Goodenough, M. J. Therien, Electron spin relaxation of hole and electron polarons in π-conjugated porphyrin arrays: Spintronic implications. *J. Phys. Chem. B* **119**, 7681–7689 (2015).
21. K. Susumu, P. R. Frail, P. J. Angiolillo, M. J. Therien, Conjugated chromophore arrays with unusually large hole polaron delocalization lengths. *J. Am. Chem. Soc.* **128**, 8380–8381 (2006).
22. J. Rawson, P. J. Angiolillo, M. J. Therien, Extreme electron polaron spatial delocalization in π-conjugated materials. *Proc. Natl. Acad. Sci. U.S.A.* **112**, 13779–13783 (2015).
23. C. Ikeda *et al.*, Helicity induction and two-photon absorbance enhancement in zinc(II) meso-meso linked porphyrin oligomers via intermolecular hydrogen bonding interactions. *J. Am. Chem. Soc.* **127**, 534–535 (2005).
24. V. S.-Y. Lin, S. G. DiMagno, M. J. Therien, Highly conjugated, acetylenyl bridged porphyrins: New models for light-harvesting antenna systems. *Science* **264**, 1105–1111 (1994).
25. P. J. Angiolillo, V. S.-Y. Lin, J. M. Vanderkooi, M. J. Therien, EPR spectroscopy and photophysics of the lowest photoactivated triplet state of a series of highly conjugated (Porphinato)Zn arrays. *J. Am. Chem. Soc.* **117**, 12514–12527 (1995).
26. R. Kumble, S. Palese, V. S.- Y. Lin, M. J. Therien, R. M. Hochstrasser, Ultrafast dynamics of highly conjugated porphyrin arrays. *J. Am. Chem. Soc.* **120**, 11489–11498 (1998).
27. I. V. Rubtsov, K. Susumu, G. I. Rubtsov, M. J. Therien, Ultrafast singlet excited-state polarization in electronically asymmetric ethyne-bridged bis[(porphinato)zinc(II)] complexes. *J. Am. Chem. Soc.* **125**, 2687–2696 (2003).
28. T. V. Duncan, K. Susumu, L. E. Sinks, M. J. Therien, Exceptional near-infrared fluorescence quantum yields and excited-state absorptivity of highly conjugated porphyrin arrays. *J. Am. Chem. Soc.* **128**, 9000–9001 (2006).
29. T. V. Duncan, P. P. Ghoroghchian, I. V. Rubtsov, D. A. Hammer, M. J. Therien, Ultrafast excited-state dynamics of nanoscale near-infrared emissive polymersomes. *J. Am. Chem. Soc.* **130**, 9773–9784 (2008).
30. T. V. Duncan, P. R. Frail, I. R. Miloradovic, M. J. Therien, Excitation of highly conjugated (porphinato)palladium(II) and (porphinato)platinum(II) oligomers produces long-lived, triplet states at unit quantum yield that absorb strongly over broad spectral domains of the NIR. *J. Phys. Chem. B* **114**, 14696–14702 (2010).
31. M. Nappa, J. S. Valentine, The influence of axial ligands on metalloporphyrin visible absorption spectra. Complexes of tetraphenylporphinatozinc. *J. Am. Chem. Soc.* **100**, 5075–5080 (1978).
32. I. Tabushi, S. Kugimiya, M. G. Kinnaird, T. Sasaki, Artificial allosteric system. 2. Cooperative 1-methylimidazole binding to an artificial allosteric system, zincgable porphyrin-dipyridylmethane complex. *J. Am. Chem. Soc.* **107**, 4192–4199 (1985).
33. N. Berova, L. Di Bari, G. Pescitelli, Application of electronic circular dichroism in configurational and conformational analysis of organic compounds. *Chem. Soc. Rev.* **36**, 914–931 (2007).
34. M. J. Frisch *et al.*, *Gaussian 16 Rev. A.03* (Gaussian, Inc., Wallingford, CT, 2016).
35. N. Berova, K. Nakanishi, R. W. Woody, *Circular Dichroism: Principles and Applications* (Wiley-VCH, New York, NY, 2000).
36. V. S.-Y. Lin, M. J. Therien, The role of porphyrin-to-porphyrin linkage topology in the extensive modulation of the absorptive and emissive properties of a series of ethynyl- and butadiynyl-bridged bis- and tris(porphinato)zinc chromophores. *Chem. Eur. J.* **1**, 645–651 (1995).
37. M. Rickhaus *et al.*, Single-acetylene linked porphyrin nanorings. *J. Am. Chem. Soc.* **139**, 16502–16505 (2017).
38. B. P. Bloom, B. M. Graff, S. Ghosh, D. N. Beratan, D. H. Waldeck, Chirality control of electron transfer in quantum dot assemblies. *J. Am. Chem. Soc.* **139**, 9038–9043 (2017).
39. C. Kulkarni *et al.*, Highly efficient and tunable filtering of electrons' spin by supramolecular chirality of nanofiber-based materials. *Adv. Mater.* **32**, 1904965 (2020).
40. A. K. Mondal *et al.*, Spin filtering in supramolecular polymers assembled from achiral monomers mediated by chiral solvents. *J. Am. Chem. Soc.* **143**, 7189–7195 (2021).
41. F. Evers *et al.*, Theory of chirality induced spin selectivity: Progress and challenges. arXiv [Preprint] (2021). https://arxiv.org/abs/2108.09998 (Accessed 21 November 2021).
42. J. Fransson, Vibrational origin of exchange splitting and chiral-induced spin selectivity. *Phys. Rev. B* **102**, 235416 (2020).
43. R. Naaman, Y. Paltiel, D. H. Waldeck, Chiral induced spin selectivity gives a new twist on spin-control in chemistry. *Acc. Chem. Res.* **53**, 2659–2667 (2020).
44. E. Z. B. Smolinsky *et al.*, Electric field-controlled magnetization in GaAs/AlGaAs heterostructures-chiral organic molecules hybrids. *J. Phys. Chem. Lett.* **10**, 1139–1145 (2019).
45. J. Bosson, G. M. Labrador, C. Besnard, D. Jacquemin, J. Lacour, Chiral near-infrared fluorophores by self-promoted oxidative coupling of cationic helicenes with amines/enamines. *Angew. Chem. Int. Ed. Engl.* **60**, 8733–8738 (2021).
46. M. Eckshtain-Levi *et al.*, Cold denaturation induces inversion of dipole and spin transfer in chiral peptide monolayers. *Nat. Commun.* **7**, 10744 (2016).